Key Points:

- Computational modeling quantifies the influence of pore space topology on S-wave propagation in volcanic rocks
- Amount, size and location of pores impact ultrasonic wave propagation in dry rocks independently of porosity
- Path effects dominate the waveforms and depend on the location of the pores

Supporting Information:

Supporting Information may be found in the online version of this article.

Correspondence to:

L. De Siena,
ldesiena@uni-mainz.de

Pore Space Topology Controls Ultrasonic Waveforms in Dry Volcanic Rocks

Maria Del Pilar Di Martino[1,2] , **Luca De Siena[3,4]** , and **Nicola Tisato[5]**

[1]School of Geosciences, University of Aberdeen, Aberdeen, UK, [2]WASM: Mineral, Energy and Chemical Engineering, Curtin University, Perth, Australia, [3]Institute of Geosciences, Johannes Gutenberg University Mainz, Mainz, Germany, [4]Mainz Institute of Multiscale Modelling, Johannes Gutenberg University, Mainz, Germany, [5]Jackson School of Geosciences, The University of Texas at Austin, Austin, TX, USA

Abstract Pore space controls the mechanical and transport properties of rocks. At the laboratory scale, seismic modeling is usually performed in relatively homogeneous settings, and the influence of the pore space on the recorded wavefields is determined by rock-fluid interactions. Understanding this influence in dry rocks is instrumental for assessing the impact of pore topology on waves propagating in heterogeneous environments, such as volcanoes. Here, we simulated the propagation of shear waves as a function of pore space parameters in computational models built as proxies for volcanic rocks. The spectral-element simulations provide results comparable with ultrasonic experiments, and the outcome shows that the size, shape, volume, and location of pores impact amplitudes and phases. These variations intensify in waveform coda after multiple scattering. Our results confirm that pore topology is one of the primary regulators of the propagation of elastic waves in dry rocks regardless of porosity.

Plain Language Summary Pores control the non-elastic behavior and, in general, the petrophysical and mechanical properties of rocks. Such properties are essential to assess potential resources such as aquifers and reservoirs or hazards posed by earthquakes, volcanoes, and constructions. The factors controlling the elasticity of rocks are texture, pore space and the fluids filling the pores. While volcanoes represent a key target for rock characterization, measuring and modeling these factors in volcanic rocks remains challenging due to their intrinsic heterogeneities. In this study, we analyzed how pore space parameters influence the overall elastic properties of rocks by changing one parameter at a time. We created synthetic samples and performed computational simulations that show the individual contribution of the amount, size, location, and shape on waveform phases and amplitudes. The findings demonstrate that we can constrain the pore space in heterogeneous rocks in simple but realistic scenarios. Our results are the first step to provide computationaly-driven forward models of seismic signals in heterogeneous volcanic media, necessary to predict the responses of volcanic rocks to stress.

1. Introduction

Linking elastic properties of rocks with pore-space parameters is a longstanding focus when characterizing hydrocarbon reservoirs, exploring geothermal resources, assessing volcanic and hydrothermal processes, and applying CO_2 sequestration techniques. This link requires evaluating the role of pore space for permeability models (e.g., Sarout, 2012) and characterizing carbonate rocks (e.g., Baechle et al., 2008) in which pore type and shape dominate the effective rock properties (Xu & Payne, 2009). The pore structure is also relevant in civil and geotechnical engineering, where pore size distribution influences how waves propagate in construction materials (e.g., Zhao et al., 2014). Recent studies provide numerical algorithms to evaluate changes in pore space topology as a function of flow parameters (reactive transport—Lisitsa et al., 2020; Prokhorov et al., 2021). However, many of these studies have focused on sedimentary rocks (as main reservoirs targets) and overlooked volcanic rocks, even though large porosities characterize the latter. Recent studies have focused primarily on the fluid-rock interaction within such rocks (e.g., Adam & Otheim, 2013; Adelinet et al., 2010; Benson et al., 2008; Clarke et al., 2020; Fazio et al., 2017).

Rock physics models typically relate velocities of elastic waves with porosity (Nur et al., 1998). However, such relations are often disregarded due to variations in rock texture, comprising pore space topology and mineral composition. For natural rocks, elastic properties cannot be accurately predicted by a single pore-space property

Writing – original draft: Maria Del Pilar
Di Martino
Writing – review & editing: Maria Del
Pilar Di Martino, Luca De Siena, Nicola
Tisato

such as the porosity value, and rock physics models should include additional parameters dependent on the topology of inclusions or pores (Dou et al., 2011; Durán et al., 2019; Ju et al., 2013; Zhang & Sharma, 2005; Zhao et al., 2014). Heap and Violay (2021) recently discussed how the pore size, shape and distribution can also influence the mechanical properties and failures modes of volcanic rocks. Several theoretical models describe effective elastic moduli in media characterized by inclusions (pores) interacting with the host matrix (e.g., Kuster & Toksöz, 1974; differential effective medium—DEM: Norris, 1985; Zimmerman, 1991) and have been used to explore the influence of pores on elastic wave velocities. Berryman (1995) summarized the expressions for the most used inclusion shapes in these models, in which the interactions between pores and the background medium are limited within effective medium approximations (Adelinet & Le Ravalec, 2015; Cheng et al., 2020; Fortin & Guéguen, 2021). Dry volcanic rocks have a complex pore system characterized by large pores (or vesicles) (Shea et al., 2010) where the effective medium approaches can provide reliable estimates in case of fluid-saturation (Hurwitz et al., 2003). However, numerical modeling and analyses of phase and amplitude of elastic waves can reduce gaps between data and models in these media. When coupled with field-scale seismic modeling (e.g., Rasht-Behesht et al., 2020), they become instrumental to understanding the imaging and interpretational potential of seismic waves propagating within fluid reservoirs and melt.

Several studies have described volcanic rocks in terms of texture, porosity, permeability, elastic moduli, and ultrasonic velocities (e.g., Durán et al., 2019; Fortin et al., 2011; Heap et al., 2020; Rossetti et al., 2019; Vanorio et al., 2002). Body wave velocities have been estimated as a function of porosity and pore shape in basaltic rocks, even as a representation of Martian rocks (Heap, 2019). However, few studies have targeted the effect of pore space topology on seismic-wave propagation in volcanic rocks. Working with dry samples and separating mineral texture and fluid interactions is one approach to constraint the effect of pore space on the effective elastic properties of rocks. Pore fluids have a prevailing effect on wave velocities, hiding the effects of pore geometry on waveforms (David & Zimmerman, 2012). While fluids are often present in volcanic rocks, they are not omnipresent (e.g., Delcamp et al., 2016; Hurwitz et al., 2003; Rowley et al., 2021). Thus, such modeling might help calibrate field measurements and recognize the difference in elastic wave signatures of saturated versus dry rocks.

Volcanic rocks are usually characterized using laboratory measurements (core analysis) or microscopy (on thin sections). More recently, digital rock physics (DRP) has proven to be a good approach to estimate physical properties without compromising the samples (e.g., Andrä et al., 2013; Ikeda et al., 2020). However, DRP methods are expensive and often unavailable to researchers. Computational simulations of ultrasonic wave propagation are a non-invasive way of testing the elastic response of rocks under different scenarios. Such simulations allow unraveling the effect of pore space topology parameters on the waveforms and, in turn, on the elastic properties of the rocks. Simulations of waves can be performed at different scales, for example, from ultrasonic to sub-seismic frequencies. Apart from wave arrivals and direct amplitudes, ultrasonic waveforms present coda waves that are caused by dispersion of the coherent waves and are highly sensitive to small-scale heterogeneities (Aki, 1969). These waves are key to characterize media at all scales. For example, at the mantle scale, wave scattering marks compositional heterogeneities (e.g., Faccenda et al., 2019). In the laboratory, these heterogeneities are the pore space and mineral grains of sizes comparable with the wavelength size (e.g., Di Martino et al., 2021).

In this study, we performed computational simulations to illustrate the effect of pore space topology on the propagation of ultrasonic waves in synthetic analogs to dry volcanic rocks. We used the software SPECFEM2D (Komatitsch & Vilotte, 1998) based on the spectral element method (SEM—Tromp et al., 2008) to simulate 2D elastic wave propagation, which allows us to accurately model ultrasonic propagation in a heterogeneous medium (Rosenkrantz et al., 2019). This approach allowed us to evaluate the impact of different pore space parameters on the full ultrasonic wavefield. We simulated shear waves propagating in synthetic samples, creating a medium described by properties previously characterized in a rock sample in the laboratory. We identified the individual contributions of pores number, size, and location; the results show that the transmitted waveforms depend on the distribution and geometry of the pore structure.

2. Methods

We performed simulations of the ultrasonic wavefield in synthetic samples resembling the ultrasonic S-wave transmission method. Full wavefields were simulated using the 2D spectral-element method code SPECFEM2D (Komatitsch & Vilotte, 1998; Implementation details in Supporting Information S1 SM-1). The source is a Ricker time wavelet with a dominant frequency of 100 kHz. Sources and receivers covered a line of 13 mm length (i.e.,
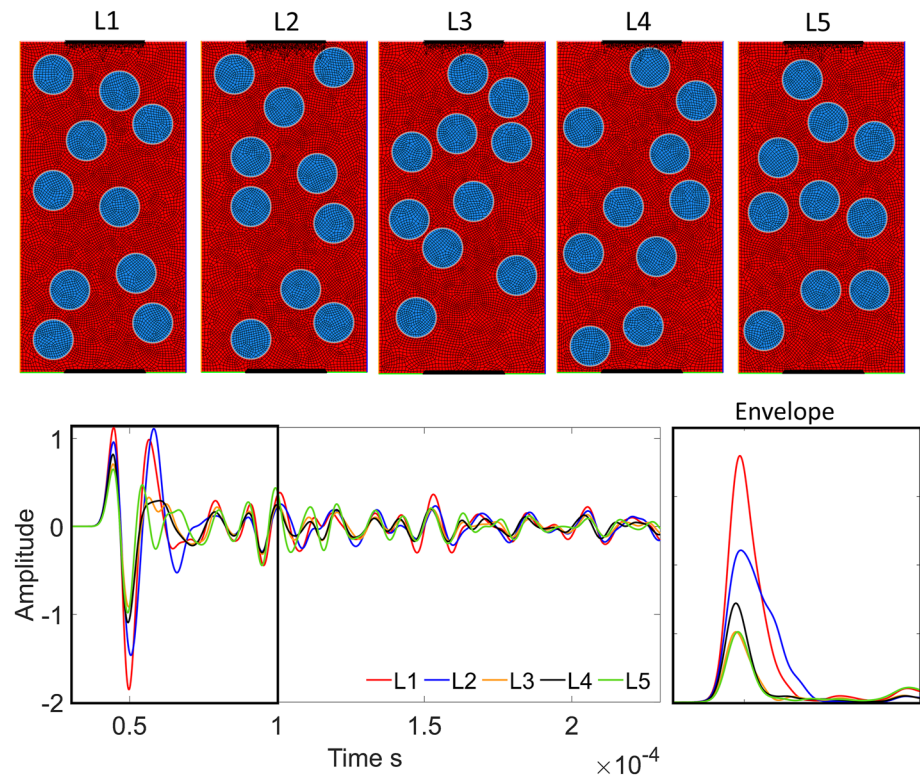
Figure 1. Simulations for Case-1. Top: synthetic samples, the rock mineral matrix occupies the red area while the void pores are the blue circles. Bottom: S-wave waveform acquired for each sample (left) and their energy envelope (right) for the first second of propagation.

half of the width of the sample), centered along the vertical axis of the sample to simulate the recording at the laboratory scale and obtain a plane-wave. In such a way, we obtained a quasi-plane wave source, where the single wavelets received at the nodes representing the receiver were averaged into one waveform.

The 2D model is rectangular (25 mm wide and 50 mm long) and represents a 2D section of a rock sample. The model is meshed using GMSH (GNU finite element mesh generator—Geuzaine & Remacle, 2009), and it includes 8,945 elements, with a maximum and minimum grid size of 0.96 and 0.11 mm, respectively. We compute waveforms of 4 ms discretized with 100,000-time steps (i.e., each step has a duration of 4 ns), satisfying the stability conditions in space for the fourth-order grid and in time for the Newmark second-order stepping scheme (Berland et al., 2006). Stacey absorbing boundary conditions (Komatitsch & Tromp, 2003; Stacey, 1988) were applied along the physical boundaries of the sample to limit reflections and conversions at the boundaries of the samples that perturbed the wave propagation. We neglect the effect of internal interactions into the sample mesh (pore-mineral interfaces) because the SPECFEM code imposes smoothness at such sharp boundaries (Rosenkrantz et al., 2019). The synthetic media mimics a basaltic rock resembling the rock sample 1H of lava flows facie in Di Martino et al. (2021). The elastic model represents a homogenous rock matrix with the elastic properties corresponding to the core rock (S-wave velocity $V_{sr} = 1,490$ m/s and density $\rho_r = 2,940$ kg/m^3), while the pores are considered free surfaces.

3. Results and Discussion

We present three case scenarios in which the geometry of the samples is constant, but their pore distribution and characteristics vary to test the hypothesis that the pore space topology controls the ultrasonic waveforms. The sensitivity of the S-waveform to pore space was investigated by changing one characteristic of the pore topology at a time. The results (Figures 1–3) correspond to SH-wave propagation in 15 synthetic samples made for 2D grid meshes, where the pore space occupies 22% of the area (i.e., representative of a sample with 22% porosity). We kept porosity constant to diminish its influence on the effective properties and to focus on the topology of the pore

space. In the same way, the aspect ratio of the pores has been kept constant ($\alpha = 1$): we represent spherical pores in all the scenarios. The amplitude (or energy) decay observed in the following results is highly associated with the ratio (λ/d) between the seismic wavelength (in this study, $\lambda = f/v = 15$ mm) and the size of the scattering heterogeneities (d-here the diameter of the pores): when $\lambda >> d$ the medium behaves like an effective homogenous medium, for $\lambda > d$ the medium falls in the Rayleigh domain, while for $\lambda \approx d$ the medium response is described by Mie scattering (Mavko et al., 2009). The Pearson correlation coefficient (cc) between the different waveforms and the energy ratio of direct and coda waves for each case quantifies the statistical relation between the samples for the three cases (see SM-2).

3.1. Case-1: Pore Location

With the first simulation, we test if the location of the pores in the sample plays a role in the transmitted waveform. This case consists of 5 wave-propagation models in synthetic samples (L1, L2, L3, L4, and L5, Figure 1) having 22% porosity and 10 pores with size $d = 6$ mm; however, pores are located randomly in the grid to evaluate the effect of the pore location on the wave propagation. The correlation coefficient between samples shows that there is a strong to very-strong correlation between the waveforms (see SM-2). The S-wave velocities, measured from the arrival time of the first break in the waveform and the propagation distance, range from 1,350.0 to 1,359.6 m/s. Waveform shapes are similar, especially in the arrival of the wave package; however, there is still a shift in phases and amplitude in the maximum of the envelope signal and the coda. To assess if the amplitude changes were driven by the closeness of the pores to the sensors, we run a similar simulation (see SM-3) in which the pores were kept at least half-wavelength away from source and receiver to remove their near-field influence on the sensor, we found that the observation is the same for both scenarios, thus validating the acquired waveforms for the study of synthetic samples. From Case-1, we conclude that the location of the pores influences ultrasonic S-wave propagation after the first arrival. The fact that the distribution of the pores into the samples can create a variation in the acquired waveforms (even a small one) strengthens the idea that pore space topology must be considered and likely modeled when analyzing the full waveform. This observation is especially relevant for applying and interpreting coda wave interferometry results in heterogeneous Earth environments, where the travel-time perturbation and changes in velocities vary with the scattering paths (Azzola et al., 2020; Snieder, 2006).

3.2. Case-2: Pore Sizes

For Case-2, we evaluated the effect of the pore size distribution by keeping constant the number and location of pores (the total porosity remains 22%). We modeled five samples (p12s1, p6s2, p4s3, p3s4, p2s6—Figure 2), having pores with sizes ranging from $d = 2.42$ to 7.82 mm, with the center of the circles located at the same position in the mesh of the five samples. The lowest correlation between waveforms was between samples p12s1 and p6s2 ($cc = 0.68$—interpreted as a moderate correlation): while p12s1 shows a quasi-homogeneous distribution of pores in space, p6s2 has two characteristics pore sizes (16% and 50% the size of the wavelength) and the larger λ/d ratio between the samples in Case-2. The correlation between samples is strong in all other cases and highest between samples p4s3 and p2s6 ($cc = 0.91$). The wave propagation in the four samples of Case-2 is affected by Mie scattering, the differences observed between the waveforms is related to the effect of the ratio λ/d on the dissipation of energy during the wave propagation. The inhomogeneity in pore sizes can redistribute energy later in the coda or dramatically increase the recorded energy (envelope of p4s3). The S-wave velocity ranges from 1,345.1 to 1,353.3 m/s, which is a close match, but after the first wavelength, there is no simple relationship between the size of the pores and the temporal redistribution of energy, with its description requiring a complete understanding of the multiple-scattering process. From Case-2, we conclude that the size of the pores has a small effect on the wave arrival time but a larger effect on direct and coda wave energies.

3.3. Case-3: Pore Number

With case-3, we confirm the hypotheses that: (a) porosity cannot predict the full-wave propagation of an elastic wave; and (b) pore space topology has a significant influence on waveforms (e.g., Di Martino et al., 2021). Case-3 consists of five wave-propagation models in synthetic samples with the same porosity but a different number of pores randomly placed in the samples. The samples named N4, N8, N16, N32, and N64 have 4, 8, 16, 32, and
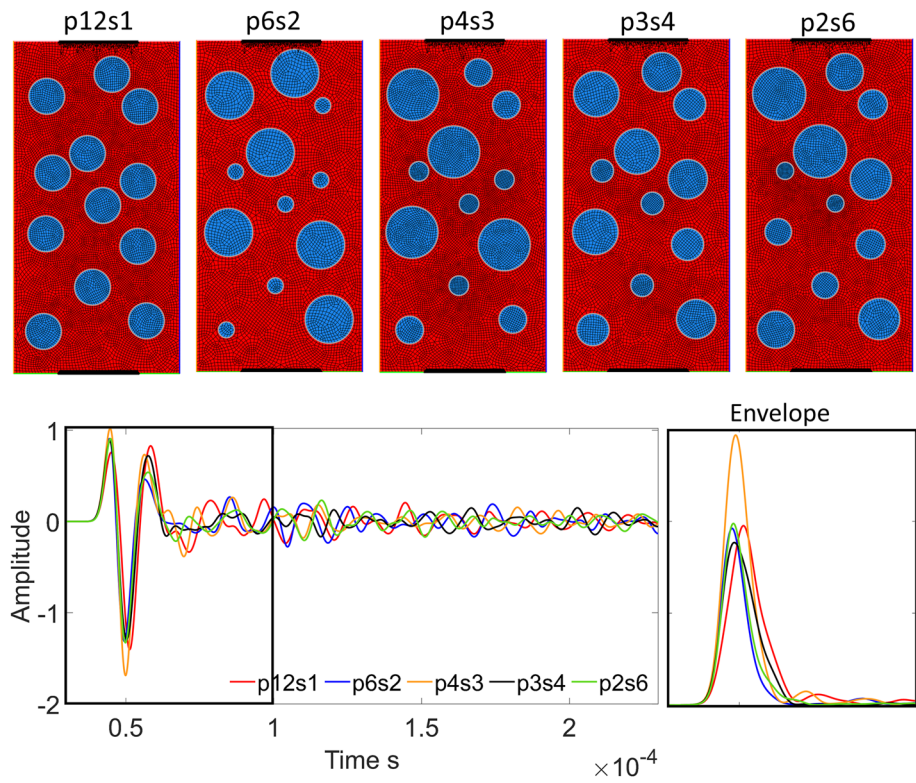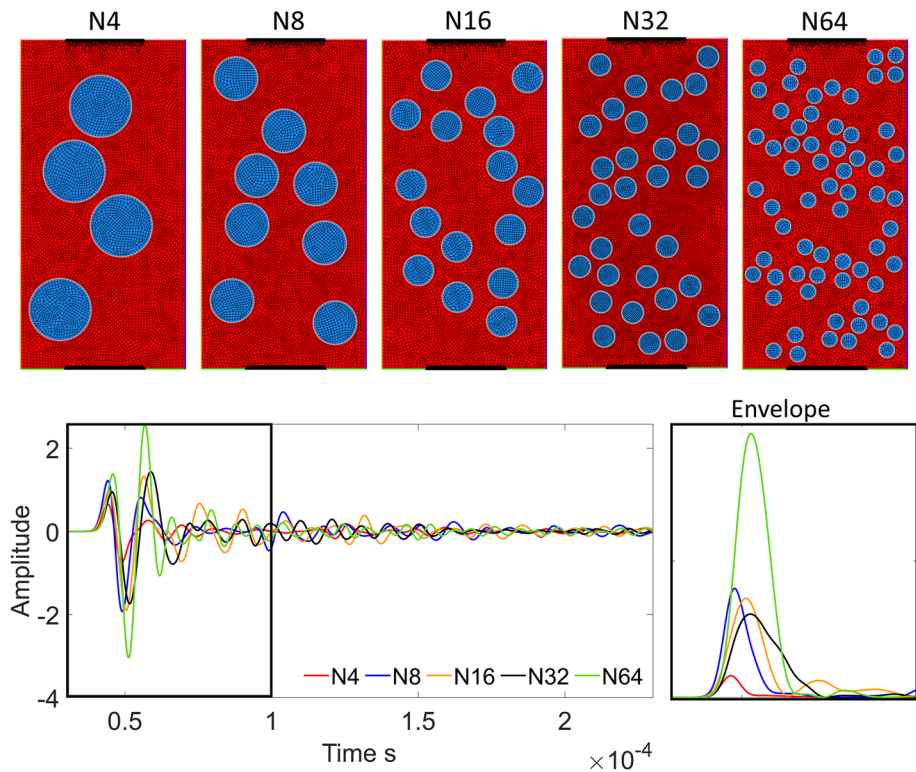
Figure 2. Same as Figure 1 for Case-2.

Figure 3. Same as Figure 1 for Case-3.

64 pores, respectively (Figure 3). To keep the porosity constant, the pore sizes are different between the samples but constant in each sample, with diameters ranging between 2.34 and 9.4 mm. Therefore, the elastic response of Case-3 samples can be described by different scattering theories.

The recorded waveforms vary considerably with the number of pores (Figure 3), indicating that the wave propagation in samples with the same porosity varies considerably with pore distribution. The lack of a progressive, smooth increase of the maximum amplitudes or phases with the number of pores (Figure 3) shows that the location and dimension of pores matter even when wavelengths are of the order of the sample dimension. The amplitude changes dramatically for sample N64: the density and small size of the pores (d = 2.34 mm) make this sample behave as an effective homogenous medium with a short correlation length. Then the measured amplitude is a strong function of the reflection coefficient, the product of the proximity of the pores to the source and the receiver. This observation trades off with the high number of pores that work as scattering points, changing amplitudes and phases of the propagating wave dramatically close to the limit of the Rayleigh scattering domain ($\lambda/d \approx 2\pi$). There is no gradual increase in amplitudes between the other samples (N4, N8, N16, N32), whose elastic responses are better described by Mie scattering. For sample N4, in which the pores have the largest size d = 9.40 mm, we observe the lowest amplitude, suggesting that the presence of large pores (vesicles) has the strongest effect on phase and amplitude variations. The results for sample N64 can be associated with those obtained for a periodic structure in triangular lattices with metamaterials or arrangements of cavities with sub-wavelength (smaller than half the wavelength) spacing (Colombi et al., 2016). In these arrangements, the inclusions are not considered scatterers but resonators (Achaoui et al., 2013). They are often studied under effective media approximations, with some composites presenting both a Bragg scattering (originated from the structure) and local resonances (Kaina et al., 2013). Further analysis of porous samples with periodic structures could offer more insights into these processes.

The correlation coefficient between samples shows that there is a weak-to-moderate correlation between the waveforms (see SM-2). The S-wave velocity ranges from 1,302 to 1,362 m/s, a variation change much larger than the maximum one (10 m/s) observed in Cases 1 and 2. From Case-3, we conclude that, for rock samples of equal porosity, the acquired waveforms are different when the samples have a different number of pores; however, we demonstrated that there is no simple relation between the number of pores, phases and amplitudes. Thus, porosity and the number of pores cannot describe full-wave propagation.

3.4. Case-4: Pore Space Topology Resembling the Rock Sample

In Case-4, we simulate the wave propagation in a rock sample mimicking the pore-space topology of the basaltic rock sample 1H (Di Martino et al., 2021). To create the mesh, we used a 2D optical image under plane-polarized light and selected the 45 largest pores (pores with an equivalent diameter smaller than 1.5 mm are not comparable with the wavelength) to relate the waveform acquired on the real sample with that obtained in a synthetic sample with spherical pores (Figure 4a, SM-4). In this case, the mesh comprises 136,854 elements, with a maximum and minimum grid size of 0.21 and 0.013 mm, respectively. We computed a waveform of 3 ms using 800,000-time steps with a duration of 0.38 ns each. The area occupied by each of the pores was estimated using ImageJ (Rasband, 2018). Spherical pores of the same area were placed in the grid, mimicking their position on sample R1H. The primary differences are caused by the shape (sphericity level) of the pores as: (a) the locations of the pores have the lowest impact on the waveform shape (Case-1); and (b) the number of pores and area occupied for each pore is the same for both samples. These differences are apparent in the coda, while real and synthetic S waves have similar direct wave packets.

Figure 4b, which summarizes our results, shows that the estimated velocities are lower than those predicted with theoretical models (Kuster & Toksöz, 1974, called K&T in Figure 4, see SM-5). The observations (R1H) cannot be reproduced by the same models as: (a) they describe effective media, which is not the case here given the large size of the pores; (b) they are developed for inclusions with specific aspect ratios (like spheres, disk, and penny cracks), which are not representatives of the shapes of the pores found in natural volcanic rocks; and (c) they assume that the pores act as isolated heterogeneities, while our methodology can handle the stress field between heterogeneities close to each other.

It is necessary to use numerical simulations to constrain or predict the elastic behavior of porous samples. However, a simple replica of the amount, location, and size of the pores can fit the S-wave packet in this simple scenario (Figure 4). Forward modeling travel time and direct-wave amplitude information, thus inverting for pore space, is possible with a relatively simple physical description and ready-to-use computational tools, like SPECFEM2D (Komatitsch & Vilotte, 1998). On the other hand, the analysis of coda waves is more complicated.
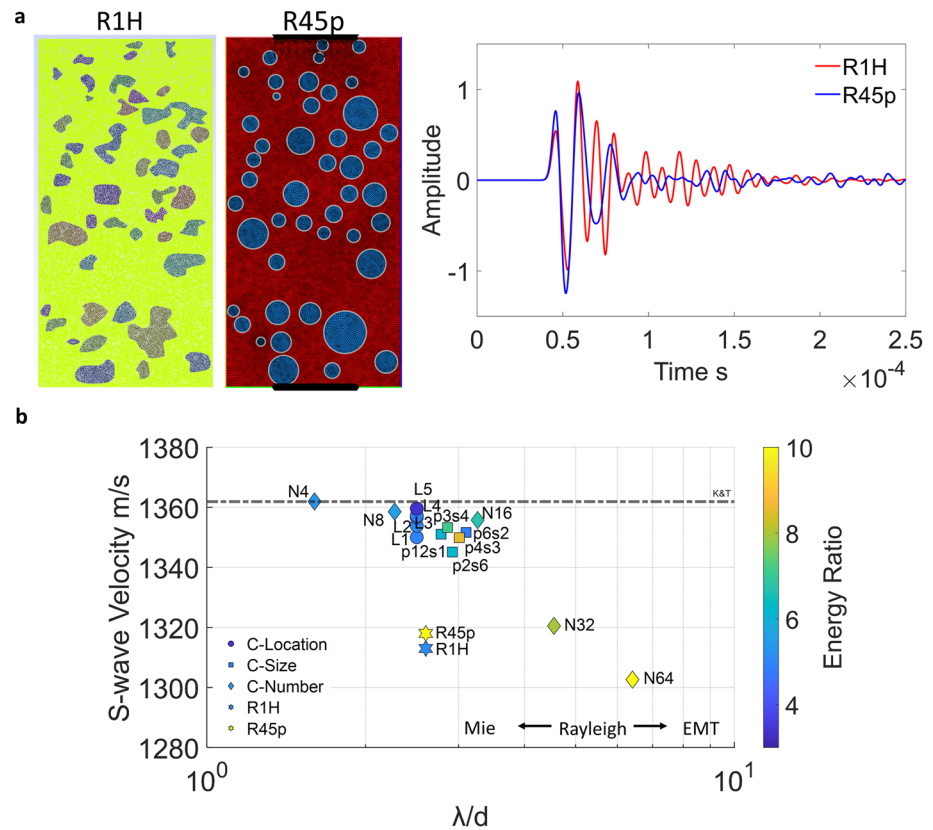
Figure 4. (a) *S*-wave propagation in a synthetic sample representing the rock sample 1H. In R1H the pore space is reconstructed from digital images while in R45p is simulated; (b) Velocity versus λ/d (λ: wavelength, d: average diameter of the pores in the sample). The color scale represents the ratio between the energy in the main wave package and the coda waves. The dashed line indicates the K&T bound, while the maximum expected velocity is ~1,687 m/s. The range of the λ/d axis going toward Mie scattering and effective medium theories (EMT) is shown for reference.

The non-sphericity of the pores increases reverberations in the early coda, slightly increasing peak delays, but it also drastically reduces peak amplitudes at later times (e.g., before and after 150 μs in Figure 4a). Energy ratios for R1H and R45p differ despite having similar S-wave velocities (1,312 and 1,318 m/s respectively, Figure 4b). These results have major consequences on the potential, applicability and interpretation of techniques using scattering as a primary physical trigger at rock and field scales, such as seismic interferometry (Azzola et al., 2020; Snieder, 2006) or absorption imaging (Sketsiou et al., 2020).

From Case-4 we conclude that it is necessary to include a pore-space representative of a realistic propagation medium when analyzing the full waveform because coda waves depend on the pore space geometry. Wavefront distortions are also observed at a regional scale by deviations in the wave propagation path between the source and receiver caused by the Earth's structure's heterogeneities (Magrini et al., 2020). In the same way that petrophysical parameters estimated from rock samples or outcrops represent the properties at the field scale, our results can be upscaled to the reservoir scale, helping constrain petro-elastic and seismic models.

4. Conclusions

In this study, we analyzed the pore space as the main driver of the S-wave velocity and amplitude perturbations. We defined the individual contribution of the number of pores, pore sizes and location of the pores on the acquired waveforms by using 2D synthetic samples that resemble volcaniclastic rock samples. The conclusions are that:

1. It is not solely porosity that controls elastic wave propagation in heterogeneous samples, as rock samples of equal porosity but different pore space topology produce different waveforms.
2. The size of the pores is a primary contributor to changes in S-wave propagation and therefore a trigger of the changes in direction and phase of the propagating wavefield, as suggested by scattering theories.

3. The location of the pores has the lowest impact on amplitudes and phases of the direct wave; hence its effect could be overlooked when estimating the velocity of elastic waves from ultrasonic wave propagation. However, the increased effect on later wave propagation could be of greater significance at the field scale.

4. Energy ratios change with pore space topology as coda waves are influenced by the topology of the pores more than the S-wave package.

5. The S-wave arrival is the only waveform parameter that can be satisfactorily reproduced using an average size and number of pores in a dry volcanic sample without the need for a replica of the pore network.

This work establishes explicit constraints of wave propagation modeling on dry volcanic rocks having a complex pore network. We conclude that models incorporating porosity and pore topology as separate factors must be developed to characterize volcanic materials.

Data Availability Statement

The data generated and analyzed in this study (mesh and waveforms) is publicly available at https://doi.org/10.17632/b5p54xtvv9.3.

References

Achaoui, Y., Laude, V., Benchabane, S., & Khelif, A. (2013). Local resonances in phononic crystals and in random arrangements of pillars on a surface. *Journal of Applied Physics*, *114*(10), 104503. https://doi.org/10.1063/1.4820928

Adam, L., & Otheim, T. (2013). Elastic laboratory measurements and modeling of saturated basalts. *Journal of Geophysical Research: Solid Earth*, *118*(3), 840–851. https://doi.org/10.1002/jgrb.50090

Adelinet, M., Fortin, J., Guéguen, Y., Schubnel, A., & Geoffroy, L. (2010). Frequency and fluid effects on elastic properties of basalt: Experimental investigations. *Geophysical Research Letters*, *37*(2), L02303. https://doi.org/10.1029/2009GL041660

Adelinet, M., & Le Ravalec, M. (2015). Effective medium modeling: How to efficiently infer porosity from seismic data? *Interpretation*, *3*(4), SAC1–SAC7. https://doi.org/10.1190/INT-2015-0065.1

Aki, K. (1969). Analysis of the seismic coda of local earthquakes as scattered waves. *Journal of Geophysical Research*, *74*(2), 615–631. https://doi.org/10.1029/JB074i002p00615

Andrä, H., Combaret, N., Dvorkin, J., Glatt, E., Han, J., Kabel, M., et al. (2013). Digital rock physics benchmarks—Part I: Imaging and segmentation. *Computers & Geosciences*, *50*, 25–32. https://doi.org/10.1016/j.cageo.2012.09.005

Azzola, J., Schmittbuhl, J., Zigone, D., Lengliné, O., Masson, F., & Magnenet, V. (2020). Elastic strain effects on wave scattering: Implications for coda wave interferometry (CWI). *Journal of Geophysical Research: Solid Earth*, *125*(3), e2019JB018974. https://doi.org/10.1029/2019JB018974

Baechle, G. T., Colpaert, A., Eberli, G. P., & Weger, R. J. (2008). Effects of microporosity on sonic velocity in carbonate rocks. *The Leading Edge*, *27*(8), 1012–1018. https://doi.org/10.1190/1.2967554

Benson, P. M., Vinciguerra, S., Meredith, P. G., & Young, R. P. (2008). Laboratory simulation of volcano seismicity. *Science*, *322*(5899), 249–252. https://doi.org/10.1126/science.1161927

Berland, J., Bogey, C., & Bailly, C. (2006). Low-dissipation and low-dispersion fourth-order Runge–Kutta algorithm. *Computers & Fluids*, *35*(10), 1459–1463. https://doi.org/10.1016/j.compfluid.2005.04.003

Berryman, J. G. (1995). Mixture theories for rock properties. In T. J. Ahrens (Ed.), *Rock physics and phase relations: A handbook of physical constants* (pp. 205–228). American Geophysical Union. https://doi.org/10.1029/RF003p0205

Cheng, W., Carcione, J. M., Qadrouh, A. N., Alajmi, M., & Ba, J. (2020). Rock anelasticity, pore geometry and the Biot–Gardner effect. *Rock Mechanics and Rock Engineering*, *53*(9), 3969–3981. https://doi.org/10.1007/s00603-020-02155-7

Clarke, J., Adam, L., Van Wijk, K., & Sarout, J. (2020). The influence of fluid type on elastic wave velocity and attenuation in volcanic rocks. *Journal of Volcanology and Geothermal Research*, *403*, 107004. https://doi.org/10.1016/j.jvolgeores.2020.107004

Colombi, A., Roux, P., Guenneau, S., Gueguen, P., & Craster, R. V. (2016). Forests as a natural seismic metamaterial: Rayleigh wave bandgaps induced by local resonances. *Scientific Reports*, *6*(1), 19238. https://doi.org/10.1038/srep19238

David, E. C., & Zimmerman, R. W. (2012). Pore structure model for elastic wave velocities in fluid-saturated sandstones. *Journal of Geophysical Research*, *117*(B7), B7210. https://doi.org/10.1029/2012JB009195

Delcamp, A., Roberti, G., & De Vries, B. V. W. (2016). Water in volcanoes: Evolution, storage and rapid release during landslides. *Bulletin of Volcanology*, *78*(12), 1–12. https://doi.org/10.1007/s00445-016-1082-8

Di Martino, M. D. P., De Siena, L., Healy, D., & Vialle, S. (2021). Petro-mineralogical controls on coda attenuation in volcanic rock samples. *Geophysical Journal International*, *226*(3), 1858–1872. https://doi.org/10.1093/gji/ggab198

Dou, Q., Sun, Y., & Sullivan, C. (2011). Rock-physics-based carbonate pore type characterization and reservoir permeability heterogeneity evaluation, Upper San Andres reservoir, Permian Basin, west Texas. *Journal of Applied Geophysics*, *74*(1), 8–18. https://doi.org/10.1016/j.jappgeo.2011.02.010

Durán, E. L., Adam, L., Wallis, I. C., & Barnhoorn, A. (2019). Mineral alteration and fracture influence on the elastic properties of volcaniclastic rocks. *Journal of Geophysical Research: Solid Earth*, *124*(5), 4576–4600. https://doi.org/10.1029/2018JB016617

Faccenda, M., Ferreira, A. M. G., Tisato, N., Lithgow-Bertelloni, C., Stixrude, L., & Pennacchioni, G. (2019). Extrinsic elastic anisotropy in a compositionally heterogeneous Earth's mantle. *Journal of Geophysical Research: Solid Earth*, *124*(2), 1671–1687. https://doi.org/10.1029/2018JB016482

Fazio, M., Benson, P. M., & Vinciguerra, S. (2017). On the generation mechanisms of fluid-driven seismic signals related to volcano-tectonics. *Geophysical Research Letters*, *44*(2), 734–742. https://doi.org/10.1002/2016GL070919

Fortin, J., & Guéguen, Y. (2021). Porous and cracked rocks elasticity: Macroscopic poroelasticity and effective media theory. *Mathematics and Mechanics of Solids*, *26*(8), 1158–1172. https://doi.org/10.1177/10812865211022034

Fortin, J., Stanchits, S., Vinciguerra, S., & Guéguen, Y. (2011). Influence of thermal and mechanical cracks on permeability and elastic wave velocities in a basalt from Mt. Etna volcano subjected to elevated pressure. *Tectonophysics*, *503*(1–2), 60–74. https://doi.org/10.1016/j.tecto.2010.09.028

Geuzaine, C., & Remacle, J.-F. (2009). Gmsh: A three-dimensional finite element mesh generator with built-in pre- and post-processing facilities. *International Journal for Numerical Methods in Engineering*, *0*, 1–24.

Heap, M. J. (2019). P- and S-wave velocity of dry, water-saturated, and frozen basalt: Implications for the interpretation of Martian seismic data. *Icarus*, *330*, 11–15. https://doi.org/10.1016/j.icarus.2019.04.020

Heap, M. J., Villeneuve, M., Albino, F., Farquharson, J. I., Brothelande, E., Amelung, F., et al. (2020). Towards more realistic values of elastic moduli for volcano modelling. *Journal of Volcanology and Geothermal Research*, *390*, 106684. https://doi.org/10.1016/j.jvolgeores.2019.106684

Heap, M. J., & Violay, M. E. (2021). The mechanical behaviour and failure modes of volcanic rocks: A review. *Bulletin of Volcanology*, *83*(5), 1–47. https://doi.org/10.1007/s00445-021-01447-2

Hurwitz, S., Kipp, K. L., Ingebritsen, S. E., & Reid, M. E. (2003). Groundwater flow, heat transport, and water table position within volcanic edifices: Implications for volcanic processes in the Cascade Range. *Journal of Geophysical Research*, *108*(B12), 2557. https://doi.org/10.1029/2003JB00256

Ikeda, K., Goldfarb, E. J., & Tisato, N. (2020). Calculating effective elastic properties of Berea sandstone using the segmentation-less method without targets. *Journal of Geophysical Research: Solid Earth*, *125*(6), e2019JB018680. https://doi.org/10.1029/2019JB018680

Ju, Y., Yang, Y., Peng, R., & Mao, L. (2013). Effects of pore structures on static mechanical properties of sandstone. *Journal of Geotechnical and Geoenvironmental Engineering*, *139*(10), 1745–1755. https://doi.org/10.1061/(ASCE)GT.1943-5606.0000893

Kaina, N., Fink, M., & Lerosey, G. (2013). Composite media mixing Bragg and local resonances for highly attenuating and broad bandgaps. *Scientific Reports*, *3*(1), 3240. https://doi.org/10.1038/srep03240

Komatitsch, D., & Tromp, J. (2003). A perfectly matched layer absorbing boundary condition for the second-order seismic wave equation. *Geophysical Journal International*, *154*(1), 146–153. https://doi.org/10.1046/j.1365-246X.2003.01950.x

Komatitsch, D., & Vilotte, J.-P. (1998). The spectral element method: An efficient tool to simulate the seismic response of 2D and 3D geological structures. *Bulletin of the Seismological Society of America*, *88*(2), 368–392.

Kuster, G. T., & Toksöz, M. N. (1974). Velocity and attenuation of seismic waves in two-phase media: Part I. Theoretical formulations. *Geophysics*, *39*(5), 587–606. https://doi.org/10.1190/1.1440450

Lisitsa, V., Bazaikin, Y., & Khachkova, T. (2020). Computational topology-based characterization of pore space changes due to chemical dissolution of rocks. *Applied Mathematical Modelling*, *88*, 21–37. https://doi.org/10.1016/j.apm.2020.06.037

Magrini, F., Diaferia, G., Boschi, L., & Cammarano, F. (2020). Arrival-angle effects on two-receiver measurements of phase velocity. *Geophysical Journal International*, *220*(3), 1838–1844. https://doi.org/10.1093/gji/ggz560

Mavko, G., Mukerji, T., & Dvorkin, J. (2009). *The rock physics handbook: Tools for seismic analysis of porous media* (2nd ed.). Cambridge University Press. https://doi.org/10.1017/CBO9780511626753

Norris, A. N. (1985). A differential scheme for the effective moduli of composites. *Mechanics of Materials*, *4*(1), 1–16. https://doi.org/10.1016/0167-6636(85)90002-X

Nur, A., Mavko, G., Dvorkin, J., & Galmudi, D. (1998). Critical porosity: A key to relating physical properties to porosity in rocks. *The Leading Edge*, *17*(3), 357–362. https://doi.org/10.1190/1.1437977

Prokhorov, D., Lisitsa, V., & Bazaikin, Y. (2021). Digital image reduction for the analysis of topological changes in the pore space of rock matrix. *Computers and Geotechnics*, *136*, 104171. https://doi.org/10.1016/j.compgeo.2021.104171

Rasband, W. S. (2018). *ImageJ*. U. S. National Institutes of Health. Retrieved from https://imagej.nih.gov/ij/

Rasht-Behesht, M., Huber, C., & Mancinelli, N. J. (2020). Detectability of melt-rich lenses in magmatic reservoirs from teleseismic waveform modeling. *Journal of Geophysical Research: Solid Earth*, *125*(9), e2020JB020264. https://doi.org/10.1029/2020jb020264

Rosenkrantz, E., Bottero, A., Komatitsch, D., & Monteiller, V. (2019). A flexible numerical approach for non-destructive ultrasonic testing based on a time-domain spectral-element method: Ultrasonic modeling of Lamb waves in immersed defective structures and of bulk waves in damaged anisotropic materials. *NDT & E International*, *101*, 72–86. https://doi.org/10.1016/j.ndteint.2018.10.002

Rossetti, L. M., Healy, D., Hole, M. J., Millett, J. M., De Lima, E. F., Jerram, D. A., & Rossetti, M. M. M. (2019). Evaluating petrophysical properties of volcano-sedimentary sequences: A case study in the Paraná-Etendeka large igneous province. *Marine and Petroleum Geology*, *102*, 638–656. https://doi.org/10.1016/j.marpetgeo.2019.01.028

Rowley, P., Benson, P. M., & Bean, C. J. (2021). Deformation-controlled long-period seismicity in low-cohesion volcanic sediments. *Nature Geoscience*, *14*(12), 942–948. https://doi.org/10.1038/s41561-021-00844-8

Sarout, J. (2012). Impact of pore space topology on permeability, cut-off frequencies and validity of wave propagation theories. *Geophysical Journal International*, *189*(1), 481–492. https://doi.org/10.1111/j.1365-246X.2011.05329.x

Shea, T., Houghton, B. F., Gurioli, L., Cashman, K. V., Hammer, J. E., & Hobden, B. J. (2010). Textural studies of vesicles in volcanic rocks: An integrated methodology. *Journal of Volcanology and Geothermal Research*, *190*(3–4), 271–289. https://doi.org/10.1016/j.jvolgeores.2009.12.003

Sketsiou, P., Napolitano, F., Zenonos, A., & De Siena, L. (2020). New insights into seismic absorption imaging. *Physics of the Earth and Planetary Interiors*, *298*, 106337. https://doi.org/10.1016/j.pepi.2019.106337

Snieder, R. (2006). The theory of coda wave interferometry. *Pure and Applied Geophysics*, *163*(2–3), 455–473. https://doi.org/10.1007/s00024-005-0026-6

Stacey, R. (1988). Improved transparent boundary formulations for the elastic-wave equation. *Bulletin of the Seismological Society of America*, *78*(6), 2089–2097. https://doi.org/10.1785/BSSA0780062089

Tromp, J., Komatitsch, D., & Liu, Q. (2008). Spectral-element and adjoint methods in Seismology. *Communications in Computational Physics*, *32*(1), 1–32.

Vanorio, T., Prasad, M., Patella, D., & Nur, A. (2002). Ultrasonic velocity measurements in volcanic rocks: Correlation with microtexture. *Geophysical Journal International*, *149*(1), 22–36. https://doi.org/10.1046/j.0956-540x.2001.01580.x

Xu, S., & Payne, M. A. (2009). Modeling elastic properties in carbonate rocks. *The Leading Edge*, *28*(1), 66–74. https://doi.org/10.1190/1.3064148

Zhang, X., & Sharma, P. (2005). Inclusions and inhomogeneities in strain gradient elasticity with couple stresses and related problems. *International Journal of Solids and Structures*, *42*(13), 3833–3851. https://doi.org/10.1016/j.ijsolstr.2004.12.005

Zhao, H., Xiao, Q., Huang, D., & Zhang, S. (2014). Influence of pore structure on compressive strength of cement mortar. *The Scientific World Journal*, 1–12. https://doi.org/10.1155/2014/247058

Zimmerman, R. W. (1991). Elastic moduli of a solid containing spherical inclusions. *Mechanics of Materials*, *12*(1), 17–24. https://doi.org/10.1016/0167-6636(91)90049-6